Reversibly Compressible, Highly Elastic, and Durable Graphene Aerogels for Energy Storage Devices under Limiting Conditions

Jin-Yong Hong, Bo Mee Bak, Jeong Jae Wie, Jing Kong, and Ho Seok Park**

High porosity combined with mechanical durability in conductive materials is in high demand for special applications in energy storage under limiting conditions, and it is fundamentally important for establishing a relationship between the structure/chemistry of these materials and their properties. Herein, polymer-assisted self-assembly and cross-linking are combined for reduced graphene oxide (rGO)-based aerogels with reversible compressibility, high elasticity, and extreme durability. The strong interplay of cross-linked rGO (x-rGO) aerogels results in high porosity and low density due to the re-stacking inhibition and steric hinderance of the polymer chains, yet it makes mechanical durability and structural bicontinuity possible even under compressive strains because of the coupling of directional x-rGO networks with polymer viscoelasticity. The x-rGO aerogels retain >140% and >1400% increases in the gravimetric and volumetric capacitances, respectively, at 90% compressive strain, showing reversible change and stability of the volumetric capacitance under both static and dynamic compressions; this makes them applicable to energy storage devices whose volume and mass must be limited.

1. Introduction

With the increasing demand for more lightweight, compact electronic devices, the feasibility of energy storage requiring less space and less mass is of prime importance for special applications in electric vehicle (EV), aerospace, solar/wind energy, and integrated on-chip systems.[1] Highly compressible energy storage devices that operate well under limited space[2] are expected to be adopted in these fields as long as they can deliver a substantial amount of gravimetric capacity (based on unit mass). Owing to the high power density, the long cycle lifetime, and the easy assembly into an entirely solid-state device, the electrochemical capacitors (ECs) that can store charges at the electrode/electrolyte interface[3] have been considered functional energy storage systems; these include flexible, bendable, compressible, and stretchable devices.[4] Among the essential components of ECs, the electrode is a major limiting factor in determining the performance of energy storage devices when the devices are confined by restrictive volume and mass requirements; these size restrictions arise as a result of the limiting form factors for shape versatility and the fact that performance degrades under spatial constraints.[5] To approach this problem from the standpoint of materials science, highly porous and lightweight yet compressible and compactible electrodes may be what is needed for both mass- and volume-restricted systems. This remains a critical challenge because presently available materials do not offer a viable solution; that is, highly porous and low-density materials typically deteriorate their intrinsic electrical and transport properties when they are deformed under the compressive stress of a limited space,[2] while highly dense and compact materials have difficulties in offering continuous ion pathways and facile access to storage sites.[6] Despite the high techonological demand and scientific importance, an energy storage device that can be reversibly compressible under extreme stresses while preserving gravimetric capacity has yet to be developed.

Recently, graphene aerogels consisting of a 3D macroporous architecture have come to be considered promising electrode materials for EC applications, due to a highly interconnected pore structure, fast ion and mass transfer, high percolated electronic transport, low density, and easy access to adsorption sites.[7] However, most pristine graphene aerogels tend to become deformed and lose intrinsic texture under compression due to the brittle skeletons and strong inter-sheet attractive forces.[8] Highly elastic graphene aerogels that can endure high compressive stress have been accomplished by architecturing a cellular form,[9] being grown on carbon nanotube aerogels,[10] and maximizing π–π interaction;[11] however, they have neither been achieved by the covalent chemistry of multifunctional polymers nor applied practically in highly compressible and durable energy storage devices until now. Excluding examples of deformation-tolerant graphene-aerogel-based ECs, the

---

Dr. J.-Y. Hong, B. M. Bak, Prof. H. S. Park
School of Chemical Engineering
Sungkyunkwan University (SKKU)
Suwon 440–746, Korea
E-mail: phs0727@skku.edu

Dr. J.-Y. Hong, Prof. J. Kong
Department of Electrical Engineering and Computer Science
Massachusetts Institute of Technology
Cambridge, MA 02139, USA
E-mail: jingkong@mit.edu

Dr. J. J. Wie
Department of Chemical and Biomolecular Engineering
University of Delaware
150 Academy Street, Newark, DE 19716, USA

DOI: 10.1002/adfm.201403273

previously reported ECs have not yet shown reversible compressibility, extreme durability, and enhancement of volumetric capacitance.[2] Hence, there is a critical need for developing reversibly compressible and mechanically durable ECs and for understanding the correlation between electrode structure/chemistry and charge-storage behavior under external stresses.

Herein, we demonstrate an innovative chemical approach to provide reversible compressibility, high elasticity, and mechanical durability in graphene aerogels using simple yet effective self-assembly and cross-linking chemistry. In particular, the structure and chemistry of cross-linked graphene aerogel is comprehensively investigated to understand the origin of the unique networking structure that combines high porosity with mechanical durability. In addition, the structure–property relationships are correlated with the unusual capacitive behavior under compressive strain. This work demonstrates the feasibility of highly and reversibly compressible electrode materials that can be adapted for energy storage under extremely limiting mass and volume requirements.

2. Results and Discussion

The overall procedure for fabricating two types of graphene-based aerogels via self-assembly is illustrated in **Figure 1**. An aqueous graphene oxide (GO) dispersion was assembled into a chemically converted reduced-GO (rGO) wet-gel through a conventional chemical reduction method, which was further processed by a freeze-drying method to yield rGO dry aerogel. The aggregation and organization of the rGO wet-gel is driven by both the diminished electrostatic repulsions between the GO sheets and the strengthened π–π stacking interaction during a chemical reduction triggered by hypophosphorus acid and iodine (Section S1 of the Supporting Information (SI)).[12] In contrast, cross-linked rGO (x-rGO) aerogel, which was obtained by covalently cross-linking the rGO aerogel with the water-soluble polymer, poly(vinyl alcohol) (PVA), was assembled in a different manner because of the unique interplay of rGO and PVA. In conjunction with the functionalities of GO (i.e., epoxy, hydroxyl, carbonyl, and carboxylic groups), the hydroxyl groups of PVA that are involved in the self-assembly of the rGO wet-gel allow for x-rGO to have better dispersion capability than pristine rGO in an aqueous solution, and thus, the resulting x-rGO aerogel is of lower density and higher porosity than the rGO aerogel (Figure 1a). Even during the washing and freeze-drying process, the less densely assembled, interconnecting networked structure of the x-rGO wet-gel was preserved without any observable shrinkage in a marginal range of monolithic volume. Details of the chemistry and interactions in the x-rGO aerogel will be discussed below.

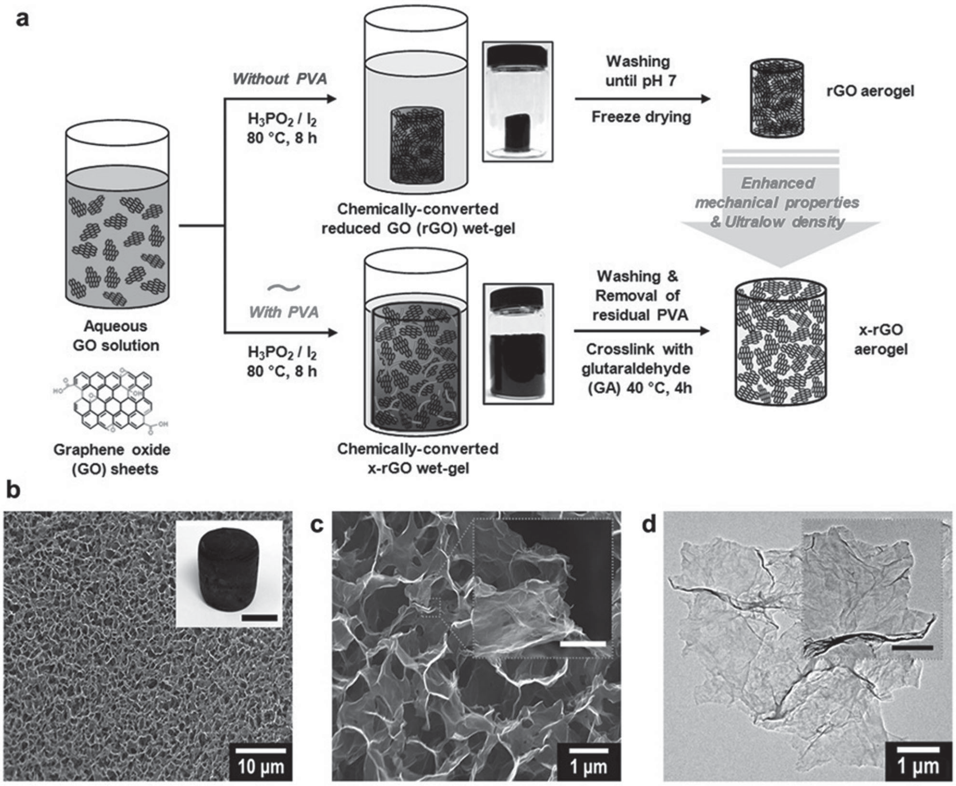

Figure 1. a) Schematic illustration of the different steps for fabricating both the rGO aerogel and x-rGO aerogel. Insets at center: Digital photographs depict the as-prepared chemically converted rGO wet-gel (top) and x-rGO wet-gel (bottom) after the self-assembly process. These wet-gels were transformed to graphene-based aerogels by a freeze-drying method. b) SEM image of the resulting x-rGO aerogel at low magnification. Inset: Digital image showing a centimeter-sized x-rGO aerogel obtained from a single reaction (scale bar is 2 cm). c) SEM images of the x-rGO aerogel at high magnification. The x-rGO aerogel exhibited uniformly interconnected pores with sizes of several micrometers. Inset scale bar is 100 nm. d) TEM images of x-rGO aerogel. Inset: high-magnification with scale bar indicating 100 nm.

The macroporous structure and nano-morphology of the x-rGO aerogel was investigated in order to confirm the PVA-assisted assembly, unlike in the formation of the rGO aerogel. A cylindrically shaped x-rGO aerogel on the scale of several centimeters was produced by one batch of the reaction; this is a very large quantity for a laboratory-scale production (Figure 1b, inset). On a micrometer scale, the 3D macropores of the x-rGO aerogel in the range of ≈0.2–1.5 μm were continuously interconnected and uniformly distributed as depicted in scanning and transmission electron microscopy (SEM and TEM) images (Figure 1b–d; Figure S1, SI). Moreover, the pore walls were composed of a single layer or a few layers of x-rGO nanosheets, whose re-stacking was prevented by the interaction of cross-linked PVA chains (insets of Figure 1c,d).

To investigate the pore characteristics of the rGO aerogel and the x-rGO aerogel, N_2 sorption measurements were performed (Figure S2 and Table S1, SI). The surface areas of the rGO and x-rGO aerogels, which were calculated by the Brunauer–Emmett–Teller (BET) equation using N_2 adsorption/desorption isotherms, were estimated to be 232.85 and 274.21 $m^2\ g^{-1}$, respectively. Interestingly, they exhibit distinct differences in their pore features (e.g., type of adsorption/desorption isotherms, pore volume, and porosity), in spite of their similar surface area. For the rGO aerogel, the isotherms fall within type-IV character with a type-H3 hysteresis loop, corresponding to typical mesoporous characteristics. However, the x-rGO aerogel showed a type-II adsorption/desorption isotherm, with a type-H3 hysteresis loop, similar to that seen for macroporous adsorbents, which is inconsistent with their micrometer-sized pore diameter (Figure S2a, SI). The different isotherm behaviors of the rGO and x-rGO aerogels are in a good agreement with the differences in pore diameter established by Barrett–Joyner–Halenda (BJH) pore distribution. In the rGO aerogel, pore volume is given by mesopores, most of them with a pore diameter of about 4 nm. For the x-rGO aerogel, macropores are dominant, with pore diameters in the range of about 10 to 200 nm (Figure S2b, SI). It was also observed that the x-rGO aerogel exhibits a relatively large pore volume and high porosity. In particular, the x-rGO aerogel has a large pore volume of 0.7889 $cm^3\ g^{-1}$ and a high porosity of 92.19% in comparison with that of the rGO aerogel (pore volume of 0.4211 $cm^3\ g^{-1}$, porosity of 84.57%). These results can be explained by the presence of extended PVA chains during the formation of the x-rGO aerogel. PVA via self-assembly plays the essential role of the inflating agent that expands the pore volume, which in turn increases the porosity of the x-rGO aerogel. Even though PVA was added at only 4.7 wt%, the interplay of rGO and PVA led to a dramatic increase in the total pore volume and porosity.

In addition, the morphology of the x-rGO features a rough nanosheet surface due to the existence of cross-linked PVA, while the rGO sheet shows a clean and flat morphology (Figure S3, SI). Such a corrugated structure of rGO enables immediate contact with PVA due to the strong polymer–nanosheet interaction, the large contact area arising from the 2D geometry of rGO, and the polymer chain mobility.

Two kinds of covalent chemistries are involved in the cross-linking of the x-rGO (**Figure 2**a): C–O–C ether bonds are formed between the oxygen-containing groups of the GO and the hydroxyl groups of PVA through esterification, and then, unreacted hydroxyl groups of the PVA chains are covalently linked with glutaraldehyde (GA) through acetalization.[13] GA was chosen for an additional cross-linking with the x-rGO aerogel because the aldehyde groups of GA selectively react with the two adjacent hydroxyl groups of PVA via acetal formation.[14] The presence of PVA in the x-rGO aerogel was confirmed by thermogravimetric analysis (TGA). The thermograms of the rGO aerogel, PVA, and the x-rGO aerogel are shown in Figure 2b. The initial weight loss of x-rGO occurring below 200 °C is attributed to the elimination of the physisorbed water molecule, while the main weight loss at around 200 °C is associated with the decomposition of the polyhydroxyl groups accompanied by depolymerization. The on-set degradation temperature of x-rGO aerogel was higher than that of pure PVA, presumably due to the strong covalent chemical interaction of rGO with PVA. The residual weight (or char yield) of the pure PVA, rGO aerogel, and x-rGO aerogel at 800 °C was estimated to be 3%, 88%, and 84%, respectively. The mass composition of the PVA component in x-rGO aerogel is calculated as follow: PVA content = (16% – 12%)/(0.97 – 0.12) = 4.7 wt%. The stoichiometric mass percentage of the PVA is therefore 4.7%, which is much less than the initially added amount (90.9%). Interestingly, all x-rGO aerogel samples prepared with various initial concentrations of PVA (1.0, 2.0, 3.0 wt%) contained a similar amount of PVA (4.3, 4.7, and 5.3 wt%, respectively). Residual PVA (not directly involved in the cross-linking reaction) could be easily removed by washing with water because of its high water solubility. The Hildebrand solubility parameters (δ) of PVA and water are 21–23 and 23.5 $cal^{0.5}\ cm^{-1.5}$, indicating a high degree of affinity.

In order to verify the chemical structure and interactions of the x-rGO, spectroscopic analyses were performed using Fourier transform infrared (FT-IR), X-ray photoemission spectroscopy (XPS), high-resolution solid-state ^{13}C magic angle spinning (MAS) nuclear magnetic resonance (NMR), and Raman spectroscopy. As expected, the x-rGO aerogel exhibited distinct IR features associated with the PVA while these peaks could not be found in the rGO aerogel. PVA was identified by its characteristic bands of $\nu_{\text{O–H stretching}}$, $\nu_{\text{C–H stretching}}$, ν_{CH2}, $\nu_{\text{C–O stretching}}$, and $\nu_{\text{C–O–C}}$ at 3280, 2930, 1420, 1142, and 1084 cm^{-1}, respectively (Figure 2c). Furthermore, the appearance of a broad peak in the region between 1000 and 1250 cm^{-1} implies that the cross-linking reactions of the rGO aerogel with PVA and GA lead to the formation of ether chemical bonds. The XPS analysis was conducted to confirm the successful reduction and cross-linking of the x-rGO aerogel (Figure 2d). The C 1s signal of GO is mainly deconvoluted into three configurations of C = C/C–C in the aromatic rings (285.0 eV), C–O (287.1 eV), and O = C–OH (288.9 eV) peaks. The C 1s spectra of the rGO aerogel revealed a drastic decrease in the intensities of the oxygen-related peaks, suggesting a high degree of reduction. In the case of the x-rGO aerogel, however, a new peak at 286.2 eV (which correspond to the C–O–C bonds) appeared, proving the formation of ether bridges during the cross-linking reaction. In addition, a full range survey scan of the x-rGO aerogel provided the composition of C at 84.96% and that of O at 8.86% (Figure S4, SI). The C/O atomic ratio of the x-rGO aerogel was approximately 9.59 for elemental analysis, slightly lower than

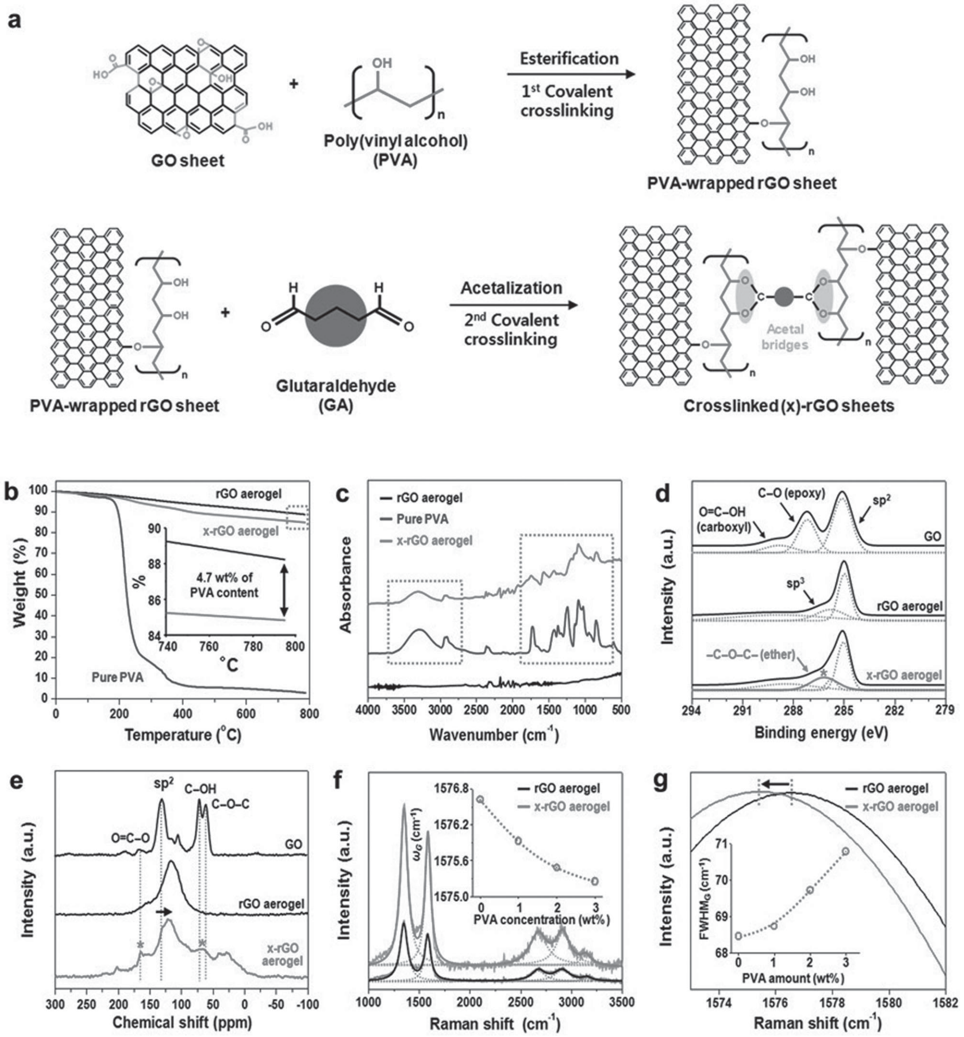

Figure 2. a) A plausible cross-linking mechanism between PVA-wrapped rGO sheets and GA. PVA-wrapped rGO sheets were covalently cross-linked by an acetal oxygen bridge. b) TGA, c) FT-IR, and d) XPS data of PVA, the rGO aerogel, and the x-rGO aerogel. In (a), the end of the TGA curve is enlarged in the inset on the right. e) ^{13}C MAS-NMR spectra with a $\pi/2$-pulse excitation of the rGO and x-rGO aerogels. f,g) Raman spectra at 532-nm excitation of the rGO aerogel (black) and x-rGO aerogel (red). f) The solid lines are the raw data, and the dotted lines are the fitted Lorentzian functions. Inset: I_D/I_G intensity ratio as a function of PVA concentration. g) Lorentzian fit curves for the G peak in the rGO aerogel (black) and x-rGO aerogel (red); inset: FWHM$_G$ values of x-rGO aerogel samples at different PVA concentrations, from 0.0 to 3.0 wt%.

that of the rGO aerogel (11.21) due to the existence of cross-linked PVA (Table S2, SI).

In order to further confirm the extent of GO reduction and cross-linking, we obtained the ^{13}C MAS-NMR spectra of the GO, rGO aerogel, and x-rGO aerogel (Figure 2e). The ^{13}C MAS-NMR spectral changes of the samples were observed after the reduction and cross-linking process. After the formation of the aerogel, the oxygen functional groups of GO at 169.3 (O = C–O), 70.7 (C–OH), and 61.3 (C–O–C) ppm remarkably disappeared, and the graphitic C sp^2 peak of GO at 130.8 ppm was up-shifted to 116.5 ppm and broadened, which is consistent with previous observations.[15] The up-shift of the graphitic C peak is due to the change in the chemical environment of the sp^2 carbons. Interestingly, some oxygen-related peaks reappeared after the chemical cross-linking reaction. The 70.0-ppm resonance is associated with hydroxylated carbons of residual PVA, and the 61.3-ppm resonance is induced by the ether bridge structure, as shown in Figure 2a.

Raman spectroscopy was used to explore the binding nature of PVA with the rGO aerogels (Figure 2f,g; Table S3, SI). Along with a peak intensity ratio for the D- and G-bands (I_D/I_G) of 1.41, the rGO aerogel exhibits a typical rGO spectrum featuring the D-band at around 1350 cm^{-1} and the G-band at around 1575 cm^{-1}. Most importantly, the G-band of the x-rGO aerogel was found to have downshifted by 1.37 cm^{-1} compared with that of the rGO aerogel (Figure 2f, inset). This downshifting phenomenon is explained as a consequence of the charge transfer between the rGO aerogel and the PVA.[16] The hydroxyl groups of PVA can donate electrons to the oxygen-containing groups on the rGO for the softening of the lattice vibration, in a similar manner to that observed in n-type doping of graphene. The full-width-at-half-maximum of the G-band (FWHM$_G$)

increases with respect to the PVA concentration (Figure 2g, inset), which is consistent with the broadening of the G-band as observed in functionalized carbon-based materials.[17] Both the increase in $\mathrm{FWHM_G}$ and the downshift of the G-band indicate the strong interaction between the rGO aerogel and PVA, and it is supported by FT-IR and NMR analyses and TEM observations. It is evident that the PVA was successfully incorporated into the interconnecting networks of the x-rGO aerogel via self-assembly, strongly interacting with rGO to retain a macroporous interconnected structure after removal of residual PVA.

Since the porous structure and physical properties of the x-rGO that are different from those of rGO originate from the interactions and chemistry of the PVA self-assembly, the role of PVA as a multifunctional polymer needs to be addressed. In other words, the origin of the high porosity and mechanical durability of x-rGO needs to be unveiled in order to understand key aspects of energy storage with requirements limiting space and mass.

First, PVA via self-assembly plays the essential role of the inflating agent; it expands pore volume, which in turn enhances the porosity of the monolithic x-rGO aerogel. As shown in the bulk density of x-rGO aerogels as a function of PVA content (**Figure 3**a), the density of the x-rGO aerogels drastically decreased and then, reached the minimum value at 4.7 wt% of PVA. This trend was visualized by the corresponding optical and SEM images of each x-rGO aerogel (Figure 3b). At the minimum of the curve in Figure 3a, the x-rGO showed the lowest density of 10.6 mg $\mathrm{cm^{-3}}$ and the highest porosity of 92.16%. However, the density of the x-rGO aerogel increased above 4.7 wt% of PVA until the 3D structure did not form due to the phase segregation of excess PVA. The PVA residues in the x-rGO aerogel remained even after the washing process, and this effect became more pronounced at a higher concentration of PVA.

The high porosity of the x-rGO aerogel can be explained by the restricted re-stacking and steric hindrance. As demonstrated by spectroscopic methods, the functional groups of PVA and rGO allow for good dispersion and full exfoliation of the rGO sheets. The substantial re-stacking of exfoliated rGO sheets was prohibited even after the construction of the 3D macroporous structure, and thus, the pore walls consisting of the x-rGO sheets became thinned out, yielding the high porosity and interconnecting network. A series of SEM images present that as the content of PVA increased, the pore walls of the x-rGO aerogel thinned and stretched while the pore size and porosity were enhanced (Figure 3c,d). In addition to the thinner wall, the diameter of the macropores was lengthened

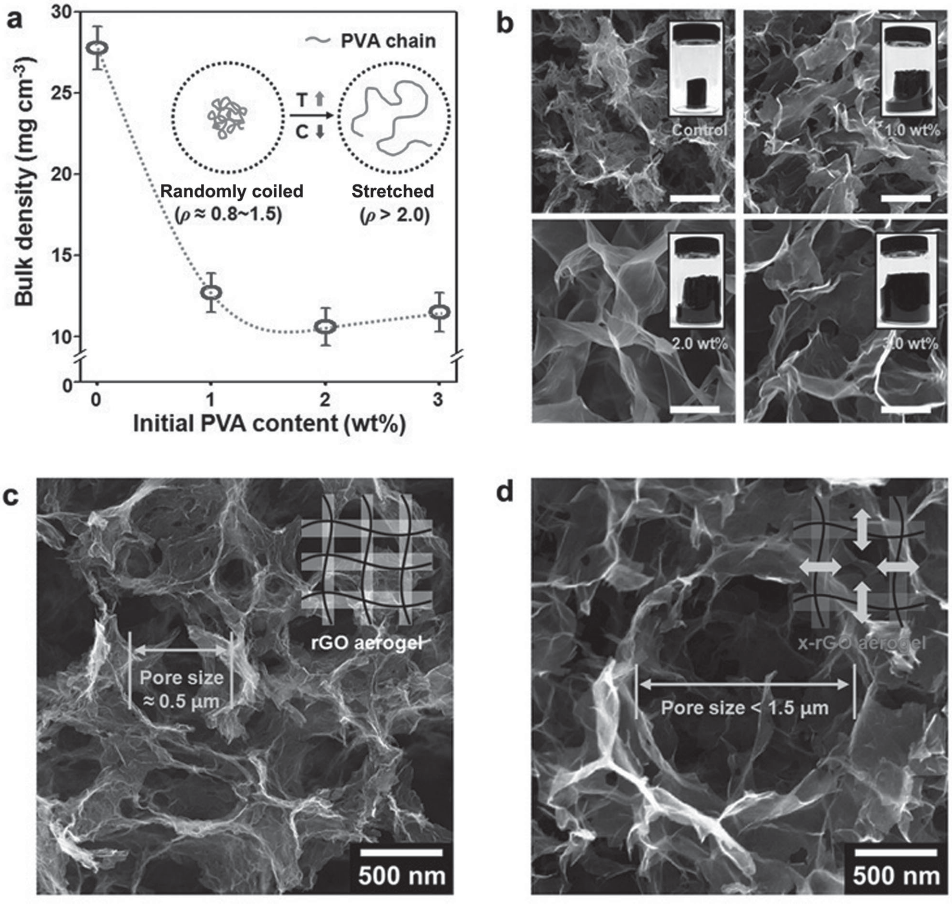

Figure 3. a) Changes in bulk density of x-rGO aerogel as a function of PVA concentration. Dashed line serves to guide the eye. Inset: Schematic representation of the PVA (M_w = 31 000 Daltons) chain structure in aqueous solution, particularly with respect to the shape factor (ρ). b) SEM images and digital photographs (insets) of x-rGO aerogels with various PVA content (labeled beneath insets); scale bars indicate 500 nm. c,d) SEM images of c) rGO aerogel and d) x-rGO aerogel prepared with PVA. Insets: Representation of PVA's role as an inflating agent in x-rGO aerogel formation.

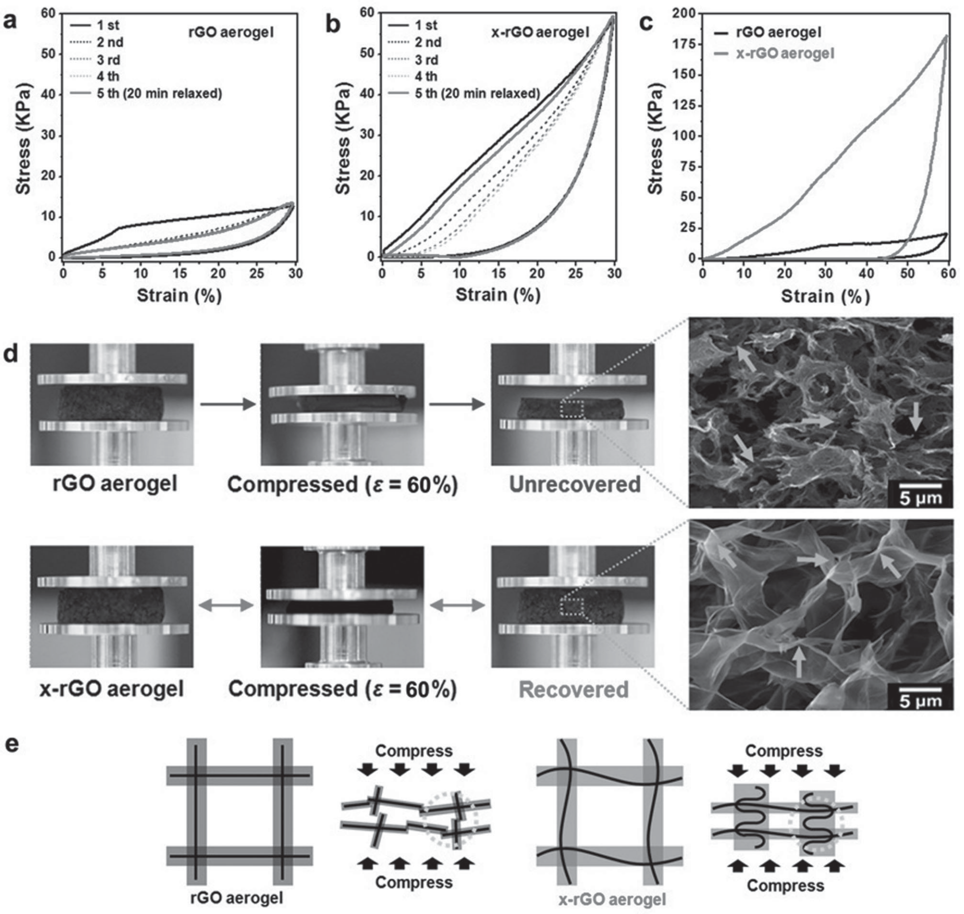

Figure 4. a,b) Compressive stress–strain curves of rGO aerogel (a) and x-rGO aerogel (b) measured by a dynamic mechanical analyzer with 30% strain in compression. Four cycles are continuously repeated, and the fifth cycle is conducted after 20 min of relaxation time. c) Compressive stress–strain curves are plotted with 60% strain for rGO (black) and x-rGO (red). d) Digital photographs and SEM images of rGO and x-rGO aerogels after compression with 60% strain. Arrows indicate the deformed and recovered region after the compression for rGO and x-rGO aerogels, respectively. e) Representation of PVA's role as a cross-linking agent in x-rGO aerogel formation.

due to the steric hindrance of PVA, contributing to the increase in the porosity of the x-rGO aerogel. The shape factor (ρ), which is defined as the ratio of the radius of gyration (R_g) to the hydrodynamic radius (R_h), of PVA in an aqueous solution was evaluated by light scattering analyses because the ρ value provides information about polymer conformation (Table S4, SI). Considering that the ρ values (≈2.0) of the PVA (weight-averaged molecular weight, M_w = 31 000 Daltons) polymer chain are indicative of a long rod-type of chain conformation, the PVA polymer (for ρ = ≈2.0) behaves as a randomly distributed rod with an aspect ratio of 43 (Section S10, SI).[18] The interactions between the PVA polymer segments and water molecules are energetically favorable for stretching the PVA polymer chains because hydrogen bonding between polymer and solvent on the main chain or side groups locks the polymer chains into an elongated conformation. As depicted in the Figure 3a inset, the PVA chains with a long-rod chain conformation exist mainly inside the pores because the R_g value of PVA (ca. 26 nm) is much smaller than the macropore diameters of the x-rGO aerogel (<1.5 μm). As the cross-linking reaction temperature increases to 80 °C, the chain mobility and freedom of segmental motion of PVA can be enhanced for a streched conformation. The elongated PVA chains with high mobility repel each other, and give sufficient steric stability against irreversible re-aggregation of the pore walls. Although the less dense interconnecting networks of the x-rGO aerogel were formed for a higher porosity than that of the rGO aerogel, the collapse of the macropores could be prevented by inflating the pore walls with the PVA chains covalently cross-linked to the rGO sheets.

The chemical cross-linking of PVA is another important contributing factor to the highly porous yet mechanically durable x-rGO aerogel since covalent chemistry offers an effective method of load transfer. Owing to the strong interatomic interactions, the mechanical properties of the x-rGO aerogels were significantly improved. The influence of the chemical cross-linking on the mechanical properties of the x-rGO aerogel was investigated by uniaxial compression tests as shown in **Figure 4**a,b. The 91.4-kPa compressive modulus for the rGO aerogel was measured in a linear elastic regime. The yield point was found at 6.8% strain (ε), where irreversible plastic deformation started to occur because the applied stress was greater than the intermolecular barriers against segmental rearrangements. Thus, the compressive modulus decreased to 45.6 ± 3.4 kPa at repeated cycles under 30% compressive strain. In contrast, a yielding behavior was not observed for the x-rGO, and its compressive modulus was 168.6 kPa, 180% greater than that of the rGO. Even in the absence of yielding, the modulus decreased during the subsequent cycles due to the viscoelasticity of the polymer, not plastic deformation. This finding is supported by the fact that the initial stress–strain curve was recovered at the fifth cycle performed after 20 min of relaxation. As expected from a previous report,[19] the effect of PVA cross-linking becomes more pronounced as the compressive strain increased to 60%. Importantly, the compressive stress of the x-rGO aerogel was 182.0 kPa, which is 8.6 times greater than that of the rGO aerogel (Figure 4c). Under compression at 50% strain, both macroscopic cracking of the rGO aerogel disk and microscopic fracturing of the sheets were observed in the optical and SEM images, respectively (Figure 4d). In contrast, both microscopic and macroscopic structures of the x-rGO aerogel remained intact due to its structural integrity.

The high compressibility of the x-rGO aerogel was further examined by means of Poisson's ratio, ν. It is known that incompressible rubber-like materials have $\nu = 0.5$ while the most compressible materials have $\nu = -1$. Assuming that the aerogel disk is uniformly expanded in a radial direction under uniaxial compression,[20] the ν values of rGO and x-rGO were measured to be 0.09 and 0.03 at 30% strain, respectively. Taking into consideration that the ν value of graphene ranges from 0.16 to 0.23, the compressibilities of both aerogels are substantially enhanced due to the interconnecting networked porous structure.[21] The threefold reduction of the ν value for x-rGO would indicate higher porosity and lower density in comparison with the rGO aerogel, and this is confirmed by the measured porosity and density.[22] Despite the low ν value, the x-rGO aerogel revealed a substantial increase in the compressive modulus (from 91.4 to 168.6 kPa) and stress (from 21.0 to 182.0 kPa) as a consequence of the cross-linking. As shown in the schematic explanation and corresponding SEM images (Figure 4e), the porous networks consisting of rGO sheets were brittle, and thus, mechanical failure was observed with 60% strain. On the other hand, the x-rGO aerogel is highly elastic and reversibly compressible, such that the original porous structure can be recovered by delocalizing the applied stresses through an effective load transfer to the covalently interconnected structures. It is worth noting that the connectivity and directional covalent bonding (or chemical cross-linking) of carbon materials result in a lower ν value.[23] As demonstrated by the decreased Poisson's ratio of the x-rGO aerogel, the connectivity and bonding strength of porous networks that are essential for highly elastic materials effectively delocalize the applied compressive stress. Accordingly, the remarkable mechanical and structural integrity of the x-rGO was attributed to the coupling of the cross-linking networks with the chemical identities of the PVA polymer and rGO nanosheet.

Taking full advantage of the highly porous yet mechanically durable x-rGO aerogels, electrochemical and capacitive behaviors were investigated using cyclic voltammetry (CV) and galvanostatic charge/discharge (GCD) curves in a three-electrode symmetric configuration and in an aqueous electrolyte (1 M H_2SO_4). The gravimetric capacitances of rGO and x-rGO aerogels for a single electrode were calculated by CV and GCD curves. The capacitance value of the x-rGO aerogels with a 4.7-wt% PVA content was optimized to 295 F g^{-1}, exceeding the 122 F g^{-1} of rGO by 240% (Figure S5, SI). Both broad redox waves at 0 V and the rectangular shapes of the x-rGO aerogels were prominent, indicating fast pseudocapacitive charging/discharging triggered by the oxygen functional groups of PVA and rGO.[24] Accordingly, the gravimetric capacitance of the rGO was enhanced by the surface functional groups, and this observation was supported by the increase in the volumetric capacitance despite the ultralow density. As the sweep rate of the CV scan increased from 10 to 100 mV s^{-1} in the range of –0.3 to 0.3 V, the capacitance retention of the x-rGO aerogels was ≈80% because of the fast redox behavior of the oxygen-containing groups and rapid ion transport by 3D macroporosity (Figure S6, SI).

In order to widen the potential window of x-rGO-aerogel-based supercapacitors, we used an organic solution of $LiClO_4$ as the electrolyte. The x-rGO aerogel has higher specific capacitance (65 F g^{-1} at 1 A g^{-1}) for organic electrolytes than that of the rGO aerogel (43 F g^{-1} at 1 A g^{-1}), under similar conditions in aqueous 1-M H_2SO_4 electrolyte (Figure S8, SI). More specifically, the x-rGO aerogel exhibited a capacitance value in an aqueous electrolyte that was 68% that of $LiClO_4$, a value superior to the 54% of the rGO aerogel at same current density of 1 A g^{-1}. These results were attributed to the dominant pseudocapacitive behavior in acidic aqueous electrolyte and the higher ionic conductivity of an electrolyte.[25] The maximum energy density depends on the operating potential window of the electrolyte. Although the specific capacitance decreased in organic electrolytes due to the lower ionic conductivity and higher viscosity compared to aqueous electrolytes, the potential window of 0.7 V increased up to 1.8 V for the enhanced energy densities. As a consequence, the x-rGO aerogel delivered the maximum energy density of 27.65 W h kg^{-1} in $LiClO_4$, which was much greater than 4.8 W h kg^{-1} in aqueous H_2SO_4 electrolyte (Figure S8, SI).

For more practical applications, the capacitive performances were measured in a two-electrode symmetric configuration (**Figure 5**a). The compression tests were performed using a home-made instrument that can control the compressive strains of all samples. Both CV curves of rGO and x-rGO aerogels at 10 mV s^{-1} showed a near-rectangular shape corresponding to a typical capacitive feature. Despite the slight distortion of the CV curve arising from the increased electrical resistance by the PVA coating, x-rGO aerogels exhibited very stable capacitive behavior even under 50% compressive strain (Figure 5b). In contrast, the CV curve of rGO was completely distorted at the identical strain, and its gravimetric capacitance dramatically dropped to 52.5% (from 80 to 42 F g^{-1}) of the initial value under no compression. As shown in the morphological change after compression, 3D interconnected networks of rGO aerogel were demolished, which indicates failure in the percolated electron and ion transport for the dramatic depression of capacitive charge storage. Notably, 3D ultrahigh porous networks of the x-rGO aerogels remained bicontinuous and percolated even with the 50% decrease in volume. When the compressive strain increases by 60% where the compressive stress of the x-rGO aerogel is much greater than that of the rGO aerogel, the capacitance discrepancy between the two became

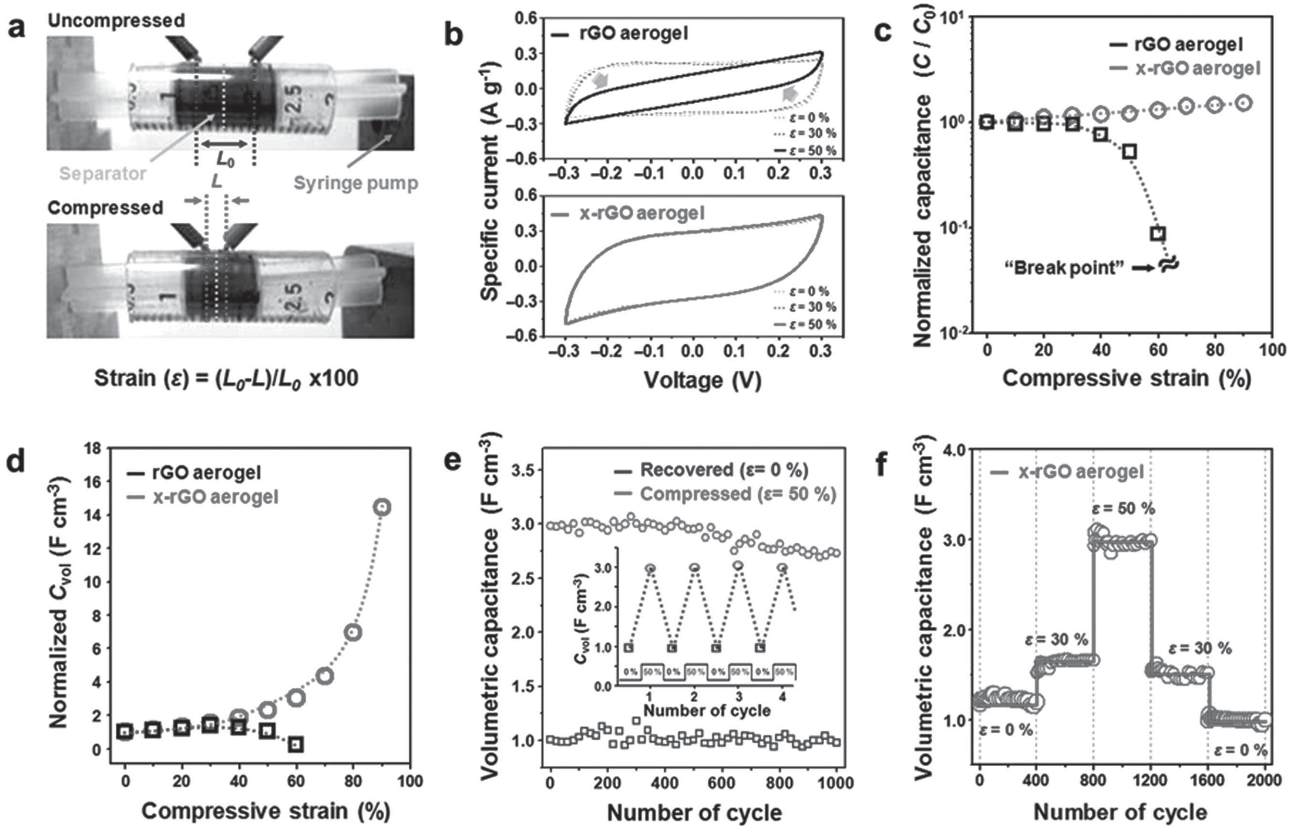

Figure 5. a) Digital photograph of the two-electrode measurement device under different compression states. Compressive strain (ε) is defined as $\varepsilon = (L_0 - L)/L_0 \times 100$, where, the L is the change in length and L_0 is initial length of x-rGO aerogel. b) Comparison between CV curves of rGO aerogel (top) and x-rGO aerogel (bottom) in original and compressed states (ε = 30 and 50%). c) Normalized gravimetric capacitances (C/C_0) and d) volumetric capacitances (C_{vol}) of rGO aerogel (black) and x-rGO aerogel (red) at compressive strains in the range of 0 to 90%. e) The C_{vol} of x-rGO aerogel under sequentially repeated compression and relaxation for 1000 cycles. f) Stability test of x-rGO aerogel. Cycle performance test showing a capacitance retention >84.5% after 2000 charging/discharging cycles under constant compression strains of 0, 30, and 50%.

more discernible (Figure 5c). Both volumetric and gravimetric capacitances of rGO were not measurable at the breaking point (~60% compressive strain). It is worth noting that the gravimetric capacitance of 90 F g^{-1} under no compression was gradually improved to 130 F g^{-1} until the maximum compressive strain of 90% was reached. As demonstrated by the 3D bicontinuous networks of x-rGO aerogels under compressive strain, the contact resistance of (electronically conductive) rGO and (electrochemically active) PVA was likely to be diminished due to volumetric shrinkage, resulting in the facile charge transport. Although the x-rGO aerogels suffered from compressive strain during a charge/discharge process, they could withstand reduction of density, which allowed the volumetric capacitance to balloon from 0.94 (0%) to 2.16 F cm^{-3} (50%). Importantly, the volumetric capacitance of x-rGO aerogels was dramatically enhanced at above 60% compressive strain, finally reaching the maximum capacitance of 13.6 F cm^{-3} (under 90% compressive strain) which is 14.5 times greater than the value of its uncompressed counterpart (Figure 5d). Such gravimetric and volumetric capacitance enhancement of x-rGO aerogels was attributed to the dense and compact yet porous and bicontinuous morphology, which was possible even under severe compression as a consequence of the effective stress delocalization of PVA cross-linked networks.

The frequency response of the x-rGO aerogels was investigated by impedance spectroscopy in order to understand the dynamics of EC devices under compressive strain (Figure S7, SI). When the comprssive strains increased, the equivalent series resistance (ESR) values of the x-rGO aerogels were reduced from 0.92 to 0.66 Ω in conjunction with the maintenance of charge transfer resistance,[26] but the rGO aerogels failed to preserve internal resistance. Moreover, the Warburg slope of the compressed x-rGO aerogels were very close to that of aerogels free of compression, whereas the slope of the rGO aerogels was reduced under compressive strain. These results find their cause in the preservation of the 3D bicontinuous network despite the compacted porous structure of x-rGO aerogels, from their own structural and mechanical integrity. Additionally, the gravimetric capacitance of the compressed x-rGO aerogels became slightly greater than that of uncompressed aerogels due to the good contact between the rGO and PVA. In contrast, the mechanical and electrochemical properties of the rGO aerogels were drastically deteriorated at above 50% of compress strain due to structural deformation (Section S15, SI).

In order to demonstrate the reversible compressibility and durability of highly elastic x-rGO aerogels, cycle stability was measured at 1 A g^{-1}. Even under both dynamic (i.e., sequentially repeated compression and relaxation) and static (i.e., constant compressive strain) conditions, no significant fluctuation of capacitance was observed. In Figure 5e, there was no significant difference of volumetric capacitance for up to 500 cycles. However, the volumetric capacitance under the compression state slightly decreased after 500 cycles, whereas the volumetric capacitance under the relaxation state was nearly constant. For long-term durability of the x-rGO aerogel, the compressive strains in the range of 0 to 50% were each varied at 400 charge/discharge cycles and finally, recovered to a fully relaxed state (Figure 5f). The initial gravimetric capacitance (110 F g^{-1}) of the x-rGO aerogel was preserved by 84.5% (93 F g^{-1}) after 2000 charge/discharge cycles under compressive strains. Impressively, the volumetric capacitances could be reversibly varied from 1.19 (free of compression) to 2.97 F cm^{-3} (50% compressive strain) due to the high elasticity and mechanical durability of the x-rGO aerogel. This finding indicates that volumetric capacitances can be increased by a factor of ≈2.4 while maintaining the gravimetric capacitance for up to even 2000 charge/discharge cycles, in spite of a decrease in the given space to half the original size.

3. Conclusion

In summary, we have demonstrated reversibly compressible and extremely durable graphene-based aerogels for energy storage where the allowed space and mass are limited. The self-assembly and cross-linking chemistries of multifunctional polymers, which offer high porosity and low density yet mechanical durability and elasticity, are highlighted in that x-rGO aerogels are highly and reversibly compressible while maintaining the 3D networked pathways for applications in ultra-compact ECs. Consequently, the x-rGO aerogel-based ECs exhibited an increase of >140% in the gravimetric capacitance and and increase of >1400% in the volumetric capacitances, even under 90% compressive strain. Furthermore, they achieved 84.5% gravimetric capacitance retention after 2000 charge/discharge cycles under static compressions as well as reversible change of volumetric capacitance under both static and dynamic modes of compressive strains due to the effective load transfer to covalent networks. As a result, their use as energy storage devices that meet limiting mass and space requirements is possible. The volumetric capacitance will be further enhanced by incorporating pseudocapacitive nanomaterials while preserving porous and durable x-rGO networks for future work.

4. Experimental Section

Fabrication of the rGO and x-rGO Aerogel: An aqueous graphene oxide (GO) solution (2.0 mg mL^{-1}), hypophosphrous acid (H_3PO_2), and iodine (I_2) were mixed at a weight ratio of 1:100:10 in a cylindrical vial at 80 °C for 8 h. After gel formation, the rGO wet-gel was taken out, washed until a pH of 7 was reached, and freeze-dried into the rGO aerogel. For the x-rGO aerogel, PVA with a M_w of 9000 Dalton (Aldrich) was dissolved in 2.0 mg mL^{-1} of aqueous GO solution and dissolved. Then, H_3PO_2 and I_2 were added at a aqueous GO solution:H_3PO_2:I_2 weight ratio of 1:100:10). The suspension was allowed to react in a cylindrical vial at 80 °C for 8 h. Finally, the x-rGO wet-gel was washed with deionized (DI) water, and treated with 0.1-wt% glutaraldehyde solution (25%, Aldrich) at 40 °C for 4 h for further chemical cross-linking. Then, it was washed again and freeze-dried.

Characterization: The morphology was confirmed using field-emission (FE)-SEM (JEOL-6700). FT-IR spectra were recorded on a FT/IR-6100 (Jasco, Japan) from 450 to 4000 cm^{-1}. Raman spectroscopy was measured on a Jobin Yvon/HORIBA spectrometer equipped with charge-coupled device (CCD) camera (1024 pixels × 256 pixels). The XPS spectra were obtained using AXIS-Ultra DLD with Al Ka (1486.6 eV). The mechanical properties were characterized by a TA Instruments dynamic mechanical analyzer (DMA, RSA3) with compression at ambient conditions. Compressive stress–strain response was measured at a strain rate of 0.05 mm s^{-1}. The TGA curves were acquired from 25 to 800 °C using argon (Ar) as a purge gas with a heating rate of 10 °C min^{-1}.

Electrochemical Measurements: The electrochemical characterization of individual electrodes was carried out in three-electrode cell with 1-M H_2SO_4 aqueous electrolyte and 1-M $LiClO_4$ organic electrolyte. The working electrode was fabricated using silver paste on a Ti foil. A platinum wire and Ag/AgCl were used as counter electrode and reference electrode, respectively. The electrochemical characterization under compressive strains was done by measuring the CV and GCD in a two-electrode configuration in 1-M H_2SO_4 electrolyte.[27] The active materials used as a current collector were prepared by slicing samples into two pieces with the same mass, using a Whatman glass microfiber filter as the separator, and immersing each sample in 1-M H_2SO_4 aqueous solutions. The symmetric devices were configured such that an aqueous-electrolyte-soaked separator was sandwiched between two electrodes. As-obtained devices were dried at room temperature before the performance measurements. All electrochemical measurements were performed using samples with the mass loading of more than 10 mg in order to avoid overestimation of specific capacitances.[28] The cyclic voltammogram was measured by a CHI760D potentiostat-galvanostat (CH Instruments Inc.) at each pressure. In addition, galvanostatic charge/discharge and impedence spectroscopy measurements were performed using a Solartron 1260.

Supporting Information

Supporting Information is available from the Wiley Online Library or from the author.

Acknowledgements

J.-Y.H. and B.M.B. contributed equally to this work. This work was supported by the GRN and Basic Science Research Programs through the National Research Foundation (NRF) funded by the Ministry of Science, ICT & Future Planning (NRF-2013S1A2A2035510 and 2011–0007677) and the Energy Efficiency & Resources of the Korea of Energy Technology Evaluation and Planning (KETEP) grant funded by the Ministry of Trade, Industry & Energy (no. 20122010100140).

Received: September 19, 2014
Revised: November 24, 2014

[1] a) P. Simon, Y. Gogotsi, *Nat. Mater.* **2008**, *7*, 845; b) J. R. Miller, *Science* **2012**, *335*, 1312; c) M. Kaempgen, C. K. Chan, J. Ma, Y. Cui, G. Gruner, *Nano Lett.* **2009**, *9*, 1872; d) J. Chmiola, C. Largeot, P.-L. Taberna, P. Simon, Y. Gogotsi, *Science* **2010**, *328*, 480; e) S.-Y. Lee, K.-H. Choi, W.-S. Choi, Y. H. Kwon, H.-R. Jung, H.-C. Shin, J. Y. Kim, *Energy Environ. Sci.* **2013**, *6*, 2414; f) Y. Meng,

Y. Zhao, C. Hu, H. Cheng, Y. Hu, Z. Zhang, G. Shi, L. Qu, *Adv. Mater.* **2013**, *25*, 2326.

[2] a) P. Li, C. Kong, Y. Shang, E. Shi, Y. Yu, W. Qian, F. Wei, J. Wei, K. Wang, H. Zhu, A. Cao, D. Wu, *Nanoscale* **2013**, *5*, 8472; b) Y. Zhao, J. Liu, Y. Hu, H. Cheng, C. Hu, C. Jiang, L. Jiang, A. Cao, L. Qu, *Adv. Mater.* **2013**, *25*, 591; c) H. Hu, Z. Zhao, W. Wan, Y. Gogotsi, J. Qiu, *Adv. Mater.* **2013**, *25*, 2219; d) Y. Tao, X. Xie, W. Lv, D.-M. Tang, D. Kong, Z. Huang, H. Nishihara, T. Ishii, B. Li, D. Golberg, F. Kang, T. Kyotani, Q.-H. Yang, *Sci. Rep.* **2013**, *3*, 2975.

[3] a) X. Wang, Y. Zhang, C. Zhi, X. Wang, D. Tang, Y. Xu, Q. Weng, X. Jiang, M. Mitome, D. Golberg, Y. Bando, *Nat. Commun.* **2013**, *4*, 2905; b) X. Wu, J. Zhou, W. Xing, G. Wang, H. Cui, S. Zhuo, Q. Xue, Z. Yana, S. Z. Qiao, *J. Mater. Chem.* **2012**, *22*, 23186; c) Z. Chen, W. Ren, L. Gao, B. Liu, S. Pei, H.-M. Cheng, *Nat Mater.* **2011**, *10*, 424; d) M. F. El-Kady, V. Strong, S. Dubin, R. B. Kaner, *Science* **2012**, *335*, 1326.

[4] a) H. Nishide, K. Oyaizu, *Science* **2008**, *319*, 737; b) V. L. Pushparaj, M. M. Shaijumon, A. Kumar, S. Murugesan, L. Ci, R. Vajtai, R. J. Linhardt, O. Nalamasu, P. M. Ajayan, *Proc. Natl Acad. Sci. USA* **2007**, *104*, 13574; c) H. Y. Jung, M. B. Karimi, M. G. Hahm, P. M. Ajayan, Y. J. Jung, *Sci. Rep.* **2012**, *2*, 773; d) L. Hu, M. Pasta, F. L. Mantia, L. Cui, S. Jeong, H. D. Deshazer, J. W. Choi, S. M. Han, Y. Cui, *Nano Lett.* **2010**, *10*, 708; e) S. Xu, Y. Zhang, J. Cho, J. Lee, X. Huang, L. Jia, J. A. Fan, Y. Su, J. Su, H. Zhang, H. Cheng, B. Lu, C. Yu, C. Chuang, T. Kim, T. Song, K. Shigeta, S. Kang, C. Dagdeviren, I. Petrov, P. V. Braun, Y. Huang, U. Paik, J. A. Rogers, *Nat. Commun.* **2013**, *4*, 1543.

[5] a) Z. Xu, Y. Zhang, P. Li, C. Gao, *ACS Nano* **2012**, *6*, 7103; b) L. Qiu, J. Z. Liu, S. L. Y. Chang, Y. Wu, D. Li, *Nat. Commun.* **2012**, *3*, 1241; c) C. Yu, C. Masarapu, J. Rong, B. Wei, H. Jiang, *Adv. Mater.* **2009**, *21*, 4793; d) X. Li, T. Gu, B. Wei, *Nano Lett.* **2012**, *12*, 6366.

[6] D. Li, R. B. Kaner, *Science* **2008**, *320*, 1170.

[7] a) S. Nardecchia, D. Carriazo, M. L. Ferrer, M. C. Gutiérrez, F. D. Monte, *Chem. Soc. Rev.* **2013**, *42*, 794; b) H. Jiang, P. S. Lee, C. Z. Li, *Energy Environ. Sci.* **2013**, *6*, 41; c) C. Li, G. Q. Shi, *Nanoscale* **2012**, *4*, 5549; d) H. S. Ahn, J.-W. Jang, M. Seol, J. M. Kim, D.-J. Yun, C. Park, H. Kim, D. H. Youn, J. Y. Kim, G. Park, S. C. Park, J. M. Kim, D. I. Yu, K. Yong, M. H. Kim, J. S. Lee, *Sci. Rep.* **2013**, *3*, 1396; e) Q. Peng, Y. Li, X. He, X. Gui, Y. Shang, C. Wang, C. Wang, W. Zhao, S. Du, E. Shi, P. Li, D. Wu, A. Cao, *Adv. Mater.* **2014**, *26*, 3241.

[8] a) M. D. Stoller, S. Park, Y. Zhu, J. An, R. S. Ruoff, *Nano Lett.* **2008**, *8*, 3498; b) C. Liu, Z. Yu, D. Neff, A. Zhamu, B. Z. Jang, *Nano Lett.* **2010**, *10*, 4863; c) S. Han, D. Wu, S. Li, F. Zhang, X. Feng, *Adv. Mater.* **2014**, *26*, 849.

[9] a) H. Huang, P. Chen, X. Zhang, Y. Lu, W. Zhan, *Small* **2013**, *9*, 1397; b) C. Hu, X. Zhai, L. Liu, Y. Zhao, L. Jiang, L. Qu, *Sci. Rep.* **2013**, *3*, 2065; c) X. Xie, Y. Zhou, H. Bi, K. Yin, S. Wan, L. Sun, *Sci. Rep.* **2013**, *3*, 2117.

[10] a) K. H. Kim, Y. Oh, M. F. Islam, *Nat. Nanotechnol.* **2012**, *7*, 562; b) Y. Zhu, L. Li, C. Zhang, G. Casillas, Z. Sun, Z. Yan, G. Ruan, Z. Peng, A.-R. O. Raji, C. Kittrell, R. H. Hauge, J. M. Tour, *Nat. Commun.* **2012**, *3*, 1225.

[11] a) Y. Li, J. Chen, L. Huang, C. Li, J.-D. Hong, G. Shi, *Adv. Mater.* **2014**, *26*, 4789; b) C. Li, G. Shi, *Adv. Mater.* **2014**, *26*, 3992.

[12] H. D. Pham, V. H. Pham, T. V. Cuong, T.-D. Nguyen-Phan, J. S. Chung, E. W. Shina, S. Kim, *Chem. Commun.* **2011**, *47*, 9672.

[13] a) H. J. Salavagione, M. A. Gómez, G. Martínez, *Macromolecules* **2009**, *42*, 6331; b) M. Cano, U. Khanb, T. Sainsbury, A. O'Neill, Z. Wang, I. T. McGovern, W. K. Masera, A. M. Benito, J. N. Coleman, *Carbon* **2013**, *52*, 363.

[14] N. Hu, L. Meng, R. Gao, Y. Wang, J. Chai, Z. Yang, E. S.-W. Kong, Y. Zhang, *Nano-Micro Lett.* **2011**, *3*, 215.

[15] a) S. Park, Y. Hu, J. O. Hwang, E.-S. Lee, L. B. Casabianca, W. Cai, J. R. Potts, H.-W. Ha, S. Chen, J. Oh, S. O. Kim, Y.-H. Kim, Y. Ishii, R. S. Ruoff, *Nat. Commun.* **2012**, *3*, 638; b) W. Cai, R. D. Piner, F. J. Stadermann, S. Park, M. A. Shaibat, Y. Ishii, D. Yang, A. Velamakanni, S. J. An, M. Stoller, J. An, D. Chen, R. S. Ruoff, *Science* **2008**, *321*, 1815; c) W. Gao, L. B. Alemany, L. Ci, P. M. Ajayan, *Nat. Chem.* **2009**, *1*, 403.

[16] Q. H. Wang, Z. Jin, K. K. Kim, A. J. Hilmer, G. L. C. Paulus, C.-J. Shih, M.-H. Ham, J. D. Sanchez-Yamagishi, K. Watanabe, T. Taniguchi, J. Kong, P. Jarillo-Herrero, M. S. Strano, *Nat. Chem.* **2012**, *4*, 724.

[17] a) K. N. Kudin, B. Ozbas, H. C. Schniepp, R. K. Prud'homme, I. A. Aksay, R. Car, *Nano Lett.* **2008**, *8*, 36; b) J. M. Englert, C. Dotzer, G. Yang, M. Schmid, C. Papp, J. M. Gottfried, H.-P. Steinrück, E. Spiecker, F. Hauke, A. Hirsch, *Nat. Chem.* **2011**, *3*, 279.

[18] T. Konishi, T. Yoshizaki, H. Yamakawa, *Macromolecules* **1991**, *24*, 5614.

[19] P. Podsiadlo, A. K. Kaushik, E. M. Arruda, A. M. Waas, B. S. Shim, J. Xu, H. Nandivada, B. G. Pumplin, J. Lahann, A. Ramamoorthy, N. A. Kotov, *Science* **2008**, *318*, 80.

[20] P. Bhupathi, L. Jaworski, J. Hwang, D. B. Tanner, S. Obukhov, Y. Lee, N. Mulders, *New J. Phys.* **2010**, *12*, 103016.

[21] a) A. Politano, A. R. Marino, D. Campi, D. Farías, R. Miranda, G. Chiarello, *Carbon* **2012**, *50*, 4903; b) R. Faccio, P. A. Denis, H. Pardo, C. Goyenola, Á. W. Mombrú, *J. Phys.: Condens. Matter* **2009**, *21*, 285304.

[22] J.-W. Jiang, J.-S. Wang, B. Li, *Phys. Rev. B* **2009**, *80*, 113405.

[23] G. N. Greaves, A. L. Greer, R. S. Lakes, T. Rouxel, *Nat. Mater.* **2011**, *10*, 823.

[24] S. K. Park, Q. Mahmood, H. S. Park, *Nanoscale* **2013**, *5*, 12304.

[25] a) Y. Chen, X. Zhang, D. Zhang, P. Yu, Y. Ma, *Carbon* **2011**, *49*, 573; b) T. Y. Kim, H. W. Lee, M. Stoller, D. R. Dreyer, C. W. Bielawski, R. S. Ruoff, K. S. Suh, *ACS Nano* **2011**, *5*, 436.

[26] B. G. Choi, J. Hong, W. H. Hong, P. T. Hammond, H. S. Park, *ACS Nano* **2011**, *5*, 7205.

[27] B. G. Choi, H. S. Park, *ChemSusChem* **2012**, *5*, 709.

[28] M. D. Stoller, R. S. Ruoff, *Energy Environ. Sci.* **2010**, *3*, 1294.